


 Cite this: *Lab Chip*, 2017, 17, 538

Versatile tissue lasers based on high-Q Fabry–Pérot microcavities†‡§

 Yu-Cheng Chen,^a Qiushu Chen,^a Tingting Zhang,^b
Wenjie Wang^b and Xudong Fan^{*ab}

Biolasers are an emerging technology for next generation biochemical detection and clinical applications. Progress has recently been made to achieve lasing from biomolecules and single living cells. Tissues, which consist of cells embedded in an extracellular matrix, mimic more closely the actual complex biological environment in a living body and therefore are of more practical significance. Here, we developed a highly versatile tissue laser platform, in which tissues stained with fluorophores are sandwiched in a high-Q Fabry–Pérot microcavity. Distinct lasing emissions from muscle and adipose tissues stained respectively with fluorescein isothiocyanate (FITC) and boron-dipyrromethene (BODIPY), and hybrid muscle/adipose tissue with dual staining were achieved with a threshold of only $\sim 10 \mu\text{J mm}^{-2}$. Additionally, we investigated how the tissue structure/geometry, tissue thickness, and staining dye concentration affect the tissue laser. Lasing emission from FITC conjugates (FITC–phalloidin) that specifically target F-actin in muscle tissues was also realized. It is further found that, despite the large fluorescence spectral overlap between FITC and BODIPY in tissues, their lasing emissions could be clearly distinguished and controlled due to their narrow lasing bands and different lasing thresholds, thus enabling highly multiplexed detection. Our tissue laser platform can be broadly applicable to various types of tissues/diseases. It provides a new tool for a wide range of biological and biomedical applications, such as diagnostics/screening of tissues and identification/monitoring of biological transformations in tissue engineering.

 Received 29th November 2016,
Accepted 5th January 2017

DOI: 10.1039/c6lc01457g

www.rsc.org/loc

1. Introduction

Biological lasers (or biolasers)¹ is an emerging field that studies lasing emission from biological and biochemical materials such as proteins,^{2–4} vitamins,⁵ luciferins,⁶ DNAs,^{7–10} cells,^{4,11–15} blood,¹⁶ and tissues^{11,17–21} when they are labelled with external fluorophores or they themselves can produce the gain media (such as in the case of fluorescent proteins).^{1,6,12,14,22,23} Advances in biolasers have demonstrated great potential in biosensing, biomedical research, and diagnosis^{4,11,20–22,24} due to their capability to amplify subtle changes in the gain media caused by underlying biological

processes, which, in combination of threshold behavior, narrow linewidth, strong lasing emission, and lasing mode spatial distribution, may lead to significant increases in detection sensitivity, multiplexibility, and imaging contrast.^{8,16,25,26} Over the past few years, biolasers have been focused mainly on the molecular level and shown significantly improved sensitivity in detecting biomolecules and their structural changes.^{3,9,27–30} More recently, biolasers using single cells with fluorescent proteins inside or externally labelled dyes/beads as the gain medium have been applied to single cell analysis.^{4,12–15} Moving beyond the molecular and cellular level, tissues, which consist of a collection of cells embedded in an extracellular matrix, are generally considered to be more practical, since they mimic the actual complex biological environment in a living body. Consequently, lasing in tissue (tissue laser) may lead to a broad range of applications in biological research, medical diagnosis, and tissue engineering.

In the past, tissue lasers have been demonstrated in the form of random lasers with a single type of fluorophore,^{17–21} showing capabilities to differentiate and sensitively analyze subtle inhomogeneities on the submicron scale.²¹ Additionally, lasing from fat tissues based on whispering-gallery modes (WGM) of natural lipid droplets in adipocytes has been achieved lately.¹³ However, random lasers rely on strong

^a Department of Biomedical Engineering, University of Michigan, 1101 Beal Ave., Ann Arbor, MI 48109, USA. E-mail: xsfan@umich.edu

^b Key Lab of Advanced Transducers and Intelligent Control System of Ministry of Education, Taiyuan University of Technology, 79 Yingze Street, Taiyuan 030024, PR China

† Y. C. and X. F. conceived the research; Y. C., Q. C., and X. F. designed the experiments; Y. C. and Q. C. performed the experiments; W. W., X. F., and T. Z. designed, fabricated, and characterized the optical mirrors and cavities; Y. C., Q. C., and X. F. analyzed data; Y. C. and X. F. wrote the paper.

‡ The authors declare no competing financial interests.

§ Electronic supplementary information (ESI) available. See DOI: 10.1039/c6lc01457g

scatters (*i.e.*, tissue inhomogeneities) to provide optical feedback for lasing and do not have a fixed cavity. Therefore, they are unable to provide predictable and trackable laser emission signals with precise locations on the tissue. In addition, the lasing characteristics (*e.g.*, intensity and threshold) vary drastically from one tissue sample to another or from one spot to another on the same tissue due to the nature of random lasers. WGM lasers, on the other hand, require the internal spherical structures of an adipocyte and thus can only be used for fat tissues. In both the random laser and the lipid droplet laser, the strong background emission from fluorophores and tissues themselves that do not participate in laser action can be coupled into the detection system (such as a spectrometer or photodetector) along with the actual lasing signal, thus considerably compromising the signal-to-background ratio (SBR) and hence the detection sensitivity

and imaging contrast. These drawbacks significantly limit the practicality and applicability of the tissue lasers.

Furthermore, detection and differentiation of specific targets (*e.g.*, cancer antibodies) in biological tissues have become a critical issue recently.^{31–33} However, the biomedical community has come to recognize that no single target analyte is likely to provide sufficient information needed to characterize a specific disease in tissues. The ability to detect multiple targets simultaneously with a higher sensitivity is therefore highly desirable.³⁴ A number of approaches have been demonstrated to achieve multiplexed detection and imaging based on fluorescence,³⁵ photoluminescence,³⁶ and Raman spectroscopy.³⁷ However, huge spectral emission overlap among fluorophores and weak signals (*i.e.*, low SBR) of Raman scattering still restrict their applications. In contrast, lasing emission can potentially provide an extremely high

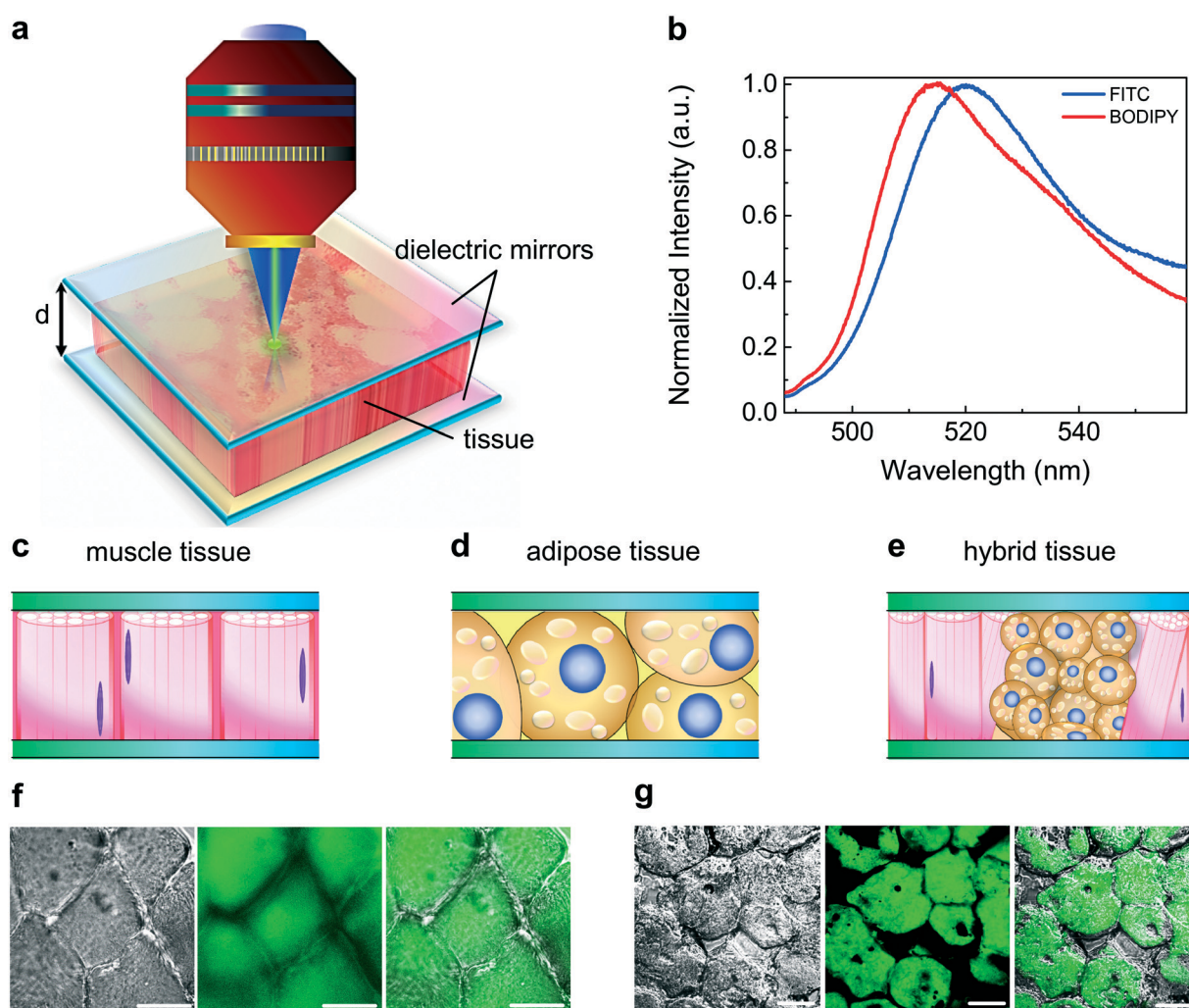


Fig. 1 Schematic showing the concept of a tissue laser. **a**, Illustration of the tissue lasing when a tissue is sandwiched within a high-Q Fabry-Pérot (FP) cavity. The thickness of tissue (*i.e.*, the cavity spacing) is denoted as d . During the experiment, the sample was excited by a pulsed optical parametric oscillator (OPO) (pulse width = 5 ns; wavelength = 465 nm). **b**, Normalized fluorescence emission spectra of FITC in water (blue curve) and BODIPY in ethanol (red curve). **c–e**, Different types of tissues investigated in this work, including muscle tissue (**c**), adipose tissue (**d**), and hybrid tissue (**e**). **f**, Microscopy images of myocytes stained with FITC (from left to right): differential interference contrast (DIC) image, confocal microscopy image, and overlap image. **g**, Microscopy images of adipocytes stained with BODIPY (from left to right): DIC image, confocal microscopy image, and overlap image. Scale bars, 20 μm .

SBR and a narrow emission band. Unfortunately, the random tissue laser in its current form is unable to detect biochemical/biological reactions from specific targets, as the underlying lasing mechanism is mainly based on the physical properties of tissues (such as inhomogeneities), whereas the lipid droplet laser can only react with and detect lipid droplets inside a cell.

These challenges motivated us to develop a new versatile tissue laser platform, in which tissues stained with various fluorophores (such as dyes, *etc.*) are sandwiched in a high- Q Fabry–Pérot (FP) microcavity, as illustrated in Fig. 1a. The fluorophores serve as the laser gain medium. Upon external excitation, the tissue laser is achieved locally around the focal spot of the pump light. In this Article, we demonstrated for the first time this FP tissue laser. Distinct lasing emissions from muscle tissue stained with fluorescein isothiocyanate (FITC), adipose tissue stained with boron-dipyrromethene (BODIPY), and hybrid muscle/adipose tissue dual-stained with FITC and BODIPY were achieved with a lasing threshold on the order of $10 \mu\text{J mm}^{-2}$ using the same pumping wavelength. We further systematically investigated the lasing characteristics of the tissue laser for various tissue structures/geometries, tissue thicknesses, and staining dye concentrations. Finally, we achieved lasing from FITC conjugated with phalloidin that specifically targets F-actin in muscle tissues.

Our studies reveal the advantages of the FP tissue laser over conventional fluorescence. Despite the large fluorescence spectral overlap (~ 100 nm) between the two fluorophores, FITC and BODIPY, lasing bands from muscle and adipose tissues can be clearly distinguished by their well separated lasing bands and different lasing threshold, thus enabling highly multiplexed spectral detection. In addition, the lasing emission has two orders of magnitude improvement in SBR over fluorescence, significantly enhancing imaging contrast. Our tissue laser platform can be readily and broadly applicable to nearly any types of tissues/diseases, and outperforms previous random tissue lasers and WGM lipid droplet lasers with a low lasing threshold, high sample-to-sample and location-to-location repeatability, high SBR, multiplexed detection capability, and the capability to target specific biomarkers in a tissue. It will open a door to a wide range of applications in medical diagnostics and screening of tissues, as well as identification and monitoring of biological transformations in tissue engineering.

2. Experimental

Optical system setup

A typical confocal setup was used to excite the sample and collect emission light from the FP cavity (Fig. 1a). In this work, a pulsed OPO laser (pulse width: 5 ns, repetition rate: 20 Hz) with a wavelength of 465 nm was used as the excitation source to excite the stained tissues with a laser beam size of $25 \mu\text{m}$ in diameter. The pump intensity was adjusted by a continuously variable neutral density filter, normally in

the average range of $1\text{--}200 \mu\text{J mm}^{-2}$. The emission light was collected through the same lens and sent to a spectrometer (Horiba iHR550, spectral resolution of ~ 0.2 nm) for analysis.

FP cavities

The FP cavity was formed by two customized dielectric mirrors (Fig. S1§). The top mirror (made by Qingdao NovelBeam Technology Co. Ltd, China) had a high reflectivity in the spectral range of 500–555 nm to provide optical feedback and high transmission around 465 nm for the pump light to pass through, whereas the bottom mirror (made by Evaporated Coatings Inc., USA) had a slightly wider reflection band. Most part of the top mirror was flat, thus forming a plano–plano (p–p) FP cavity with the flat bottom mirror. The top mirror also had an array of concave structures, made by computer-controlled CO_2 laser ablation (before dielectric coating), thus forming a plano–concave (p–c) FP cavity that has better cavity stability and higher Q -factors. The Q -factor for the p–p and p–c FP cavities was on the order of 10^4 and 10^5 , respectively, at a cavity length of $30 \mu\text{m}$ (in the absence of tissues). Details of the fabrication and characterization of the p–p and p–c FP cavities are described in ref. 38.

Tissue and device preparation

All the fresh pig tissues were obtained from a local slaughterhouse. In this work, the muscle and fat tissues were selected from pig ribs without any processing or fixing. Fresh tissues were frozen immediately and embedded into an OCT (optimal cutting temperature) compound to form an OCT tissue block under -20 °C. Tissue sections were then sliced into thin sections ($20 \mu\text{m}$, $30 \mu\text{m}$, and $40 \mu\text{m}$ in thickness) by using a cryostat (Leica 3000). Selected sections, which were first cleaned and rinsed with lysine for better tissue adhesion, were picked up and placed on the top of a poly-L-lysine (Sigma-Aldrich #P8920) coated dielectric mirror (see Fig. S1§ for details of the mirrors). Tissues were then rinsed with PBS (phosphate buffered solution, R&D Systems #841380, #896009) and air dried before staining. After staining (see details about staining in the next section) and appropriate rinsing again, the tissue was mounted with PBS and covered by the top dielectric mirror. For confocal microscopy, the tissues were first deposited on the top of a glass slide (Thermo-Fisher #3021-002), followed by the same staining process, then mounted with Fluoromount (Sigma-Aldrich #4680) and covered with a coverslip before scanning.

Staining and materials

For muscle tissues, FITC powder (Sigma-Aldrich #F6377) was dissolved in de-ionized (DI) water at a concentration of 3 mM, then diluted to lower concentrations. The FITC solution was then applied to the muscle tissue for 10 minutes, followed by rinsing with PBS solution 3 times before measurement. For adipose tissues, BODIPY (Life-Tech #D3922) was dissolved in pure ethanol at a concentration of 3 mM, then diluted to lower concentrations with ethanol. The

BODIPY solution was then applied to the adipose tissue for 20 minutes, followed by rinsing with PBS solution 3 times before measurement. For dual staining of the hybrid tissue, we first applied 2 mM FITC solution to the tissue for 10 minutes, followed by rinsing with PBS 3 times, and then 1 mM BODIPY solution for 20 minutes, followed by rinsing with PBS solution 3 times. For specific staining using FITC-phalloidin (Thermo Fisher #F432), the bulk solution was diluted with methanol to form a 10 μM solution and applied to the muscle tissue sections for 20 minutes as suggested. Then, the tissue was rinsed with PBS 3 times before measurement.

Optical imaging techniques

The differential interference contrast (DIC) and confocal fluorescence microscopy images were taken by using a Nikon A1 spectral confocal microscope with excitation of a 488 nm laser source. The bright field images of tissue lasing were captured by using a CCD (Thorlabs #DCU223C) integrated directly on top of the objective in our laser experimental setup in Fig. 1a.

3. Results and discussion

Fig. 1a illustrates the concept of the FP tissue laser. The detailed description of the experimental setup is presented in Experimental. The FP cavity was formed by two dielectric mir-

rors. The details of the mirror fabrication and characterization, as well as FP cavity assembly, can be found in Experimental and Fig. S1. We used FITC and BODIPY, the two commonly used dyes in tissue staining,^{39–41} as the exemplary gain media. Their fluorescence emission spectra are given in Fig. 1b, showing strong spectral overlap over 100 nm. Further, we chose three major types of tissues as the model system, *i.e.*, muscle tissue, adipose tissue, and hybrid tissue, as illustrated in Fig. 1c–e. FITC and BODIPY were used to stain muscle tissue (myocytes) and adipose tissue (brown adipocytes), respectively. Fig. 1f shows the DIC and confocal fluorescence microscopy images of a muscle tissue stained with FITC. Since FITC is a non-specific dye, physical absorption of dyes throughout the whole tissue takes place as the main staining mechanism. Nevertheless, it can still be clearly observed that the inner part of each myocyte was stained by more FITC due to its slight binding ability to primary amine groups of proteins.^{42,43} The DIC and confocal images of adipose tissue stained with BODIPY are given in Fig. 1g. Obviously, since BODIPY is a lipophilic stain, it labels all the lipid droplets randomly distributed throughout the whole brown adipocyte.

We first investigated the feasibility and characteristics of the tissue laser under various muscle tissue thicknesses and FITC concentrations in Fig. 2. All the muscle tissue sections were prepared so that muscle fibers (myofibrils) were in the

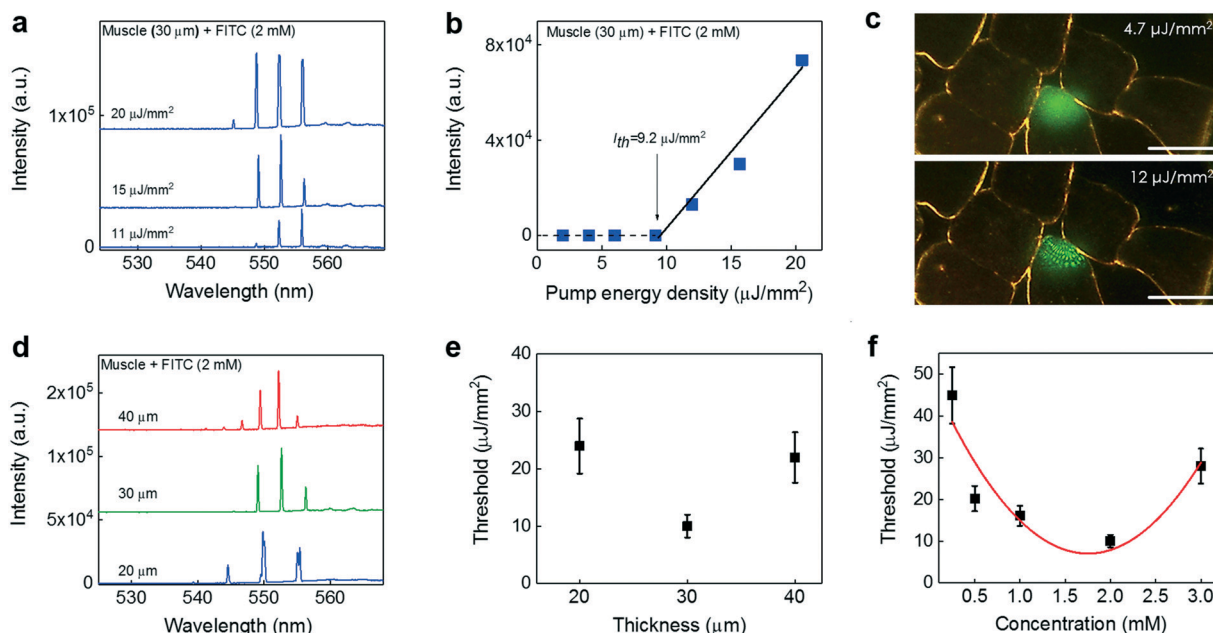


Fig. 2 Lasing in muscle tissue – longitudinal myofibrils. **a**, Examples of lasing spectra of muscle tissue (30 μm) stained with FITC (2 mM) under various pump energy densities. Curves are vertically shifted for clarity. **b**, Spectrally integrated (545–560 nm) laser output as a function of pump energy density extracted from the spectra in **a**. The solid lines are the linear fit above the lasing threshold, which is 9.2 $\mu\text{J mm}^{-2}$. **c**, CCD images of the muscle tissue laser output below (4.7 $\mu\text{J mm}^{-2}$) and above (12 $\mu\text{J mm}^{-2}$) the lasing threshold. The image clearly shows several myocytes. The laser beam was, however, focused on only one of the myocytes. Scale bars, 20 μm . **d**, Lasing spectra of muscle tissue with different section (cavity) thicknesses (**d**) at 35 $\mu\text{J mm}^{-2}$ (all of which were above the lasing threshold). Curves are vertically shifted for clarity. **e**, Laser threshold for different tissue thicknesses. The concentration of FITC used to stain the tissue was 2.0 mM. Error bars were based on three individual measurements at different sites. **f**, Laser threshold with different concentrations of FITC used to stain the tissue at the fixed tissue thickness (and hence the cavity length) of 30 μm . The solid curve is a quadratic fit to guide the eye. Error bars were based on three individual measurements at different sites. Details of the lasing spectra and threshold plots of all data points in **e** and **f** can be found in Fig. S4 and S5,§ respectively.

longitudinal direction (*i.e.*, the myofibrils were aligned perpendicularly to the mirror surface and parallel to the laser emission). The lasing spectra of a 30 μm thick muscle tissue stained with 2 mM FITC under various pump intensities are shown in Fig. 2a. Sharp and periodic lasing peaks start to emerge around 553 nm with an overall lasing band of only ~ 10 nm (545–555 nm), much narrower than the corresponding fluorescence band (>50 nm in Fig. 1b), which is typical for lasing emission.^{44–46} The spectral linewidth of each lasing peak is 0.2 nm,⁴⁶ limited by the spectrometer resolution. It should be noted that, in comparison with the lasing wavelength of pure FITC in the absence of muscle tissue (centered around 525 nm – see Fig. S2§), a 30 nm red-shift in the FITC-stained tissue laser was observed, which is due to myoglobin in muscle tissue that has a lower extinction coefficient at 555 nm than at 525 nm.⁴⁷ The spectrally integrated laser emission *versus* pump energy density extracted from Fig. 2a is presented in Fig. 2b, from which the lasing threshold is derived to be approximately $9.2 \mu\text{J mm}^{-2}$, similar to our theoretical analysis and simulation in Fig. S3a. Distinct changes in output emission below and above the threshold can be better visualized by the CCD images in Fig. 2c. Below the lasing

threshold, the emission is spatially featureless throughout the focal spot on the tissue. Above the lasing threshold, the laser output is generally described by Ince–Gaussian modes.^{48,49} Due to the quasi-circular symmetry of the myofibrils inside the cavity, the laser emission in Fig. 2c looks more like Laguerre–Gaussian modes.

We further investigated how tissue thickness and the concentration of staining FITC affect the lasing characteristics, which is important for future practical use of tissue lasers in biology and biomedicine. Fig. 2d shows the lasing spectra by varying the muscle tissue thickness with the fixed concentration of FITC used to stain the tissue (2 mM). The respective FSR for the cavity lengths of 20 μm , 30 μm , and 40 μm is 5.3 nm, 3.5 nm, and 2.7 nm, respectively, which give an average effective muscle tissue refractive index of 1.43, close to the reported value of 1.41.⁵⁰ Although the number of lasing modes increases with the increased tissue thickness due to the multimode nature of the FP cavity at the current lengths (20–40 μm), the lasing band still remains around 10 nm. Note that the slight increase in background around 560 nm (see Fig. 2a and d, as well as Fig. 5e and f) is caused by the reduced reflectivity of the dielectric mirror of the FP cavity

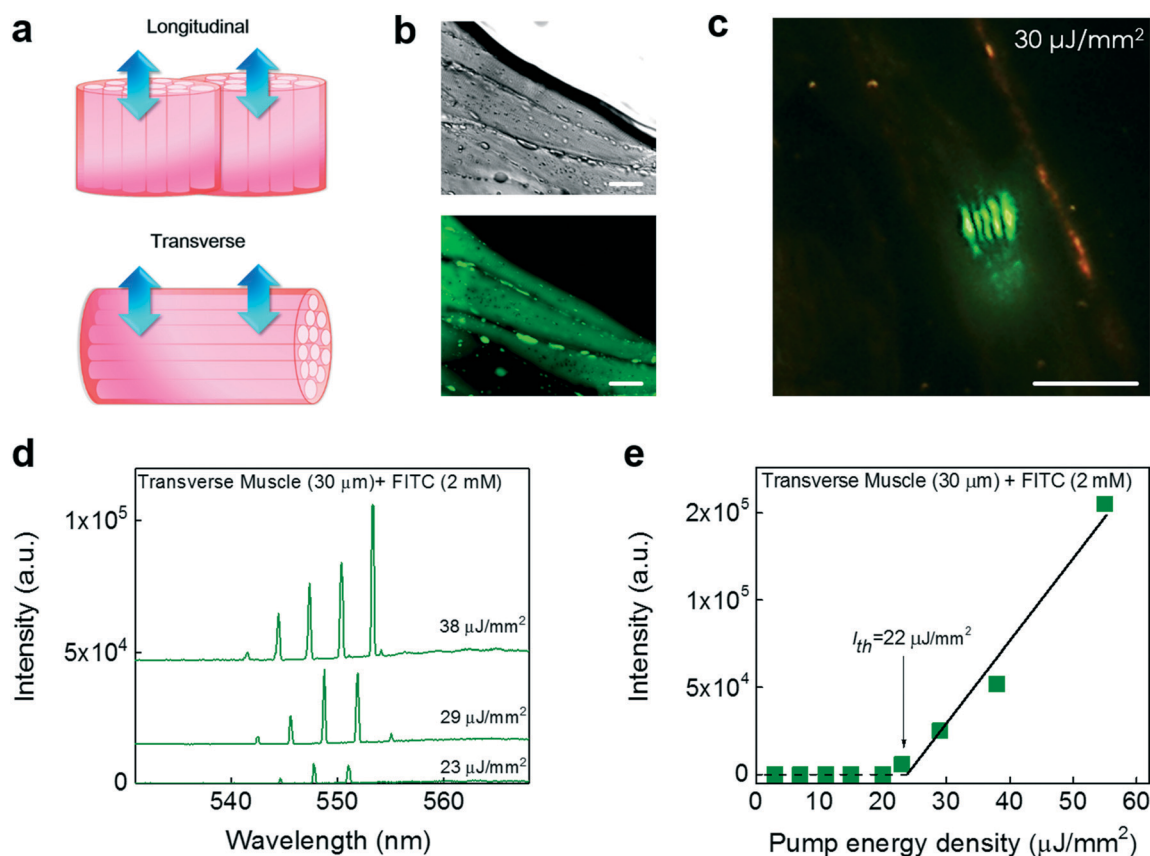


Fig. 3 Lasing in muscle tissue – transverse myofibrils. a, Schematic showing the two arrangements of myofibrils (muscle fibers), longitudinal and transverse. Arrows indicate the lasing emission direction. The FP cavity is not shown. b, DIC (upper) and confocal fluorescence microscopy (lower) images of transverse myofibrils stained with FITC. c, CCD images of tissue lasing in transverse myofibrils. d, Examples of lasing spectra of transverse muscle tissue stained with FITC under various pump energy densities. Curves are vertically shifted for clarity. e, Spectrally integrated (540–560 nm) laser output as a function of pump energy density extracted from d. The solid line is the linear fit above the threshold, showing a lasing threshold of approximately $22 \mu\text{J mm}^{-2}$. Tissue thickness = 30 μm . [FITC] = 2.0 mM. Excitation wavelength = 465 nm. All scale bars, 20 μm .

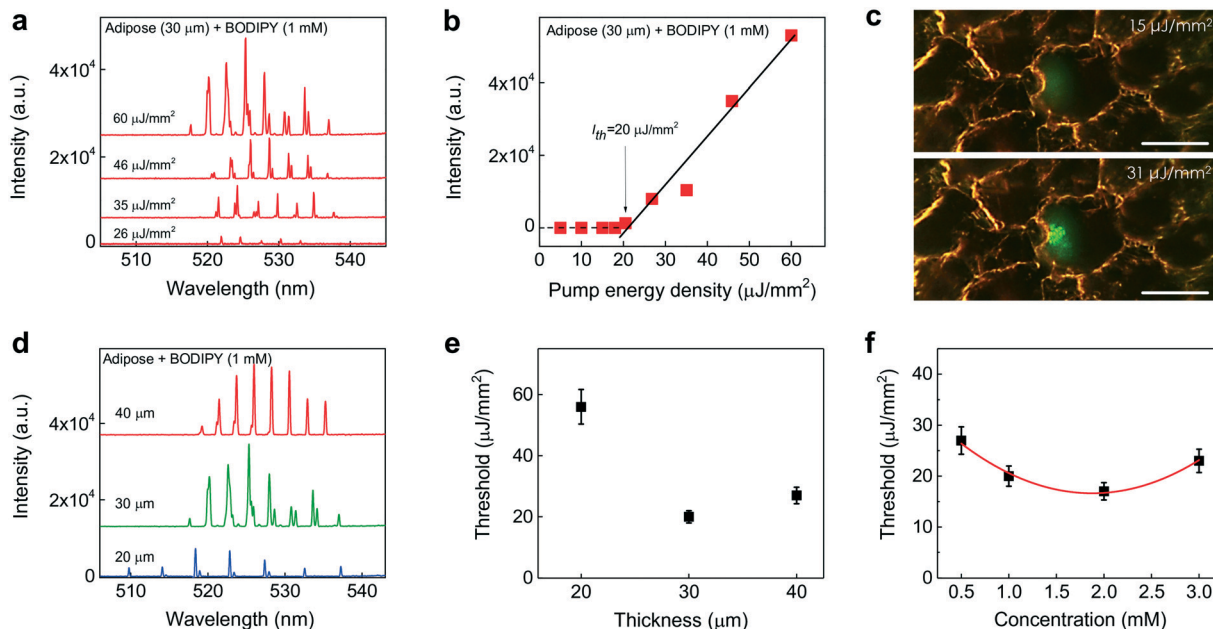


Fig. 4 Lasing in adipose tissue. **a**, Examples of lasing spectra of adipose tissue (30 μm) stained with BODIPY (1.0 mM) under various pump energy densities. Curves are vertically shifted for clarity. **b**, Spectrally integrated (520–535 nm) laser output as a function of pump energy density extracted from the spectra in **a**. The solid line is the linear fit above the lasing threshold, which is approximately 20.0 $\mu\text{J mm}^{-2}$. **c**, CCD images of the muscle tissue laser output below (15 $\mu\text{J mm}^{-2}$) and above (31 $\mu\text{J mm}^{-2}$) the lasing threshold. The image shows clear boundaries of several adipocytes, in which the laser beam is focused on only one of the fat cells. Scale bars, 20 μm . **d**, Lasing spectra of adipose tissues of different thicknesses above the lasing threshold. **e**, Laser threshold for different tissue thicknesses. The concentration of BODIPY used to stain the tissue was 1.0 mM. Error bars were based on three individual measurements at different sites. **f**, Laser threshold with different concentrations of BODIPY used to stain the tissue at the fixed tissue thickness (and hence the cavity length) of 30 μm . The solid curve is a quadratic fit to guide the eye. Error bars were based on three individual measurements at different sites. Details of the lasing spectra and threshold plots of all data points in **e** and **f** can be found in Fig. S7 and S8.†

(Fig. S1b†). Fig. 2e plots the lasing threshold of the tissue laser of various tissue thicknesses, showing that the optimal muscle tissue thickness is around 30 μm .

Furthermore, we investigated the dependence of the lasing threshold on the FITC concentration at the fixed tissue thickness (30 μm), as shown in Fig. 2f. The lasing threshold decreased monotonically when the FITC concentration used to stain the tissue increased from 0.25 mM to 2 mM. The overall agreement between the experimental results with the simulation in Fig. S3b† suggests that the concentration of FITC inside the muscle tissue follows the concentration of FITC in solution outside the tissue at an approximately 1 : 1 ratio during staining. This appears to be reasonable, as FITC molecules simply migrate into and are subsequently trapped by the tissue matrix non-specifically during staining. However, when the FITC concentration exceeds 2 mM, the threshold begins to rise again, which is due probably to the self-quenching effect of the dye at high concentrations. In fact, the FP laser with pure FITC (in the absence of the muscle tissue) shows the similar threshold decrease when the FITC concentration increases from 0.5 mM to 2 mM and the similar threshold increase when the FITC concentration increases from 2 mM to 3 mM.

In order to comprehensively understand how the tissue geometric structures affect the lasing properties and thresholds, we compared the lasing from the muscle tissue with

that of the myofibrils in the transverse and longitudinal directions (Fig. 3a). The DIC and confocal fluorescence images of transverse myofibrils stained with FITC are given in Fig. 3b. The tissue sections (30 μm) were cut from the same piece of tissue as in Fig. 2 but with different cutting directions and sandwiched in the same FP cavity. The lasing characteristics of transverse muscles exhibit a remarkable difference from those of longitudinal muscles. First, the spatial pattern of lasing emission (Fig. 3c) resembles linear Hermite–Gaussian modes due to the myofibril arrangement. Second, the lasing threshold for the transverse muscle is about 22 $\mu\text{J mm}^{-2}$ (Fig. 3d and e), approximately 2–3 times larger than that for the longitudinal muscle. The lower lasing threshold in the longitudinal muscle is due to the light-guiding (light confinement) mechanism along the myofibrils^{51,52} (see Fig. S6† to visualize the light-guiding effect) and fewer interfaces (myofibril/sarcolemma) that the light encounters when it travels between the two mirrors.

To demonstrate the versatility of our tissue laser platform, we further studied the lasing properties of brown adipose tissue stained with BODIPY, as shown in Fig. 4. The lasing spectra of a 30 μm brown adipose tissue stained with 1 mM BODIPY under various pump energy densities are shown in Fig. 4a. Periodic lasing peaks start to emerge around 528 nm and the overall lasing band is approximately 15 nm (520–535 nm), still much narrower than the corresponding

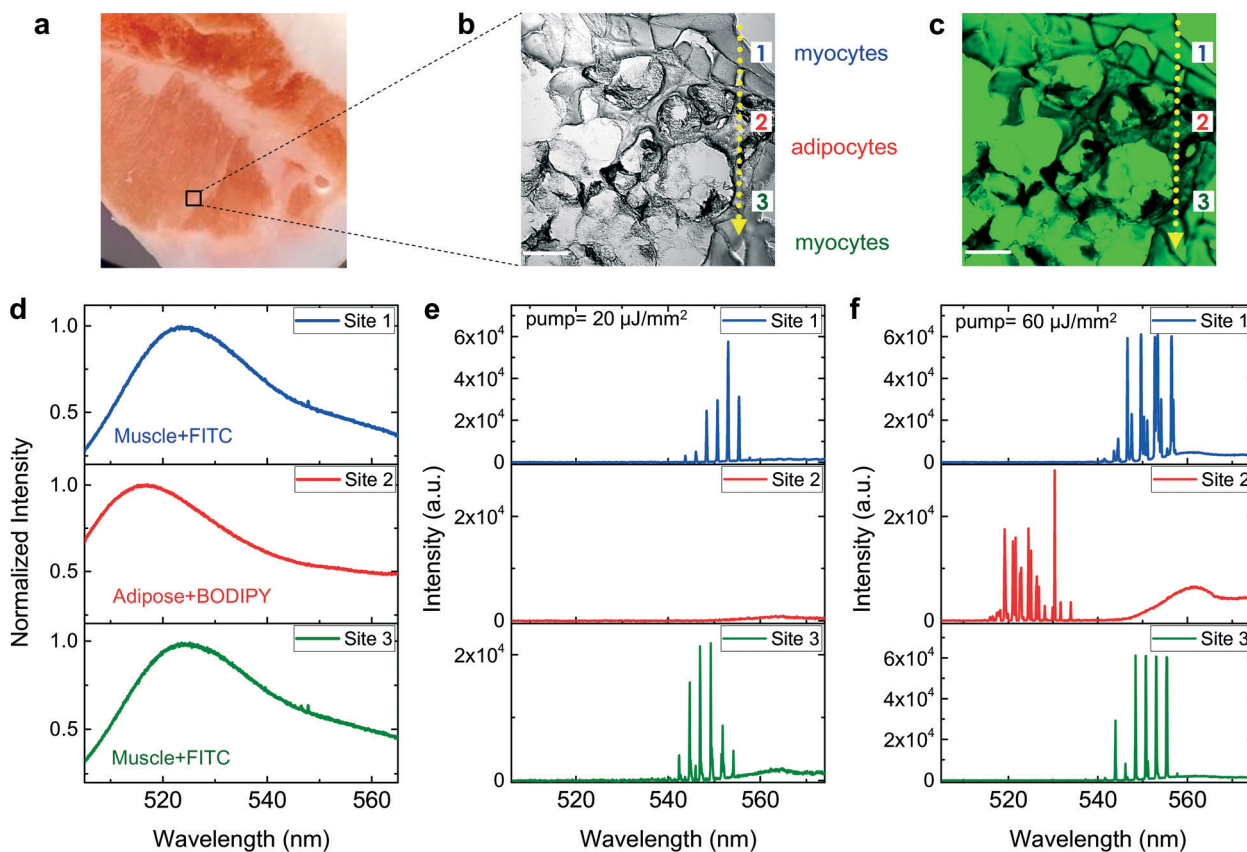


Fig. 5 Multiplexed lasing in hybrid tissue. **a**, A photo of the piece of hybrid tissue used in this experiment. The labeled black square is the region of interest where muscle tissues and adipose tissues cannot be distinguished directly by their appearance. **b**, DIC image of the hybrid tissue labeled in **a** containing an irregular mixture of adipose tissues and muscle tissues. Three representative sites were taken on (site 1) muscle tissue, (site 2) adipose tissue, and (site 3) muscle tissue, respectively, as the pump laser beam scanned through one direction (see the dashed arrows). **c**, Confocal image of the hybrid tissue dual-stained with FITC and BODIPY. **d**, Fluorescence spectra of muscle tissue with FITC (site 1), adipose tissue with BODIPY (site 2), and muscle tissue with FITC (site 3). **e**, Lasing spectra taken at sites 1, 2, and 3, respectively, when the pump energy density was set between the threshold for muscle tissue and that for adipose tissue ($20 \mu\text{J mm}^{-2}$). **f**, Lasing spectra taken at sites 1, 2, and 3, respectively, when the pump energy density was above the threshold for both muscle tissue and adipose tissue ($60 \mu\text{J mm}^{-2}$). Note that the increase in the background emission spectra around 560 nm in **e** and **f** is due to the fluorescence leaking out of the FP cavity caused by the reduced reflectivity of the dielectric mirror (see Fig. S1b§ for details). Scale bars in **b** and **c**, $40 \mu\text{m}$.

fluorescence band. Due to the absence of myoglobin, the lasing band of the adipose tissue is red-shifted only 10 nm with respect to that from pure BODIPY lasing (see Fig. S2§), much smaller than the 30 nm red-shift observed for the muscle laser discussed previously. The spectrally integrated laser emission *versus* pump energy density presented in Fig. 4b shows the lasing threshold of approximately $20 \mu\text{J mm}^{-2}$. Prominent changes in output emission below and above the threshold were obtained through the CCD images in Fig. 4c. Below the lasing threshold ($15 \mu\text{J mm}^{-2}$), the emission is spatially featureless throughout the focal spot on the tissue. Above the lasing threshold ($31 \mu\text{J mm}^{-2}$), the spatial output exhibits more irregular patterns than that for the muscle tissues arranged longitudinally or transversely, because of various sizes of lipid droplets randomly distributed within the focal point of the pump light.

The effects of tissue thickness and BODIPY concentration on the lasing characteristics were also studied. Fig. 4d shows the lasing spectra for various tissue thicknesses with the

BODIPY concentration fixed at 1 mM. The measured FSR for the cavity lengths of $20 \mu\text{m}$, $30 \mu\text{m}$, and $40 \mu\text{m}$ is 4.5 nm, 2.9 nm, and 2.2 nm, respectively, which result in an average effective tissue refractive index of 1.55, close to the reported value of 1.48.^{50,53} The lasing threshold for various tissue thicknesses is shown in Fig. 4e, showing the optimal tissue thickness of about $30 \mu\text{m}$, similar to that for the muscle tissue. Fig. 4f shows the dependence of the lasing threshold on the BODIPY concentration at a fixed adipose tissue thickness. The lasing threshold decreased gradually between 0.5 mM and 2 mM. However, due to the self-quenching effect of BODIPY, the lasing threshold rises when the concentration exceeds 2 mM, which is also similar to what we observed for the muscle tissue with FITC.

After studying individual dyes with individual types of tissues, we further achieved selective and multiplexed lasing from a hybrid tissue (Fig. 5a), which allows us to generate lasing signals from myocytes and adipocytes on the same piece of tissue. The tissue was dual-stained, *i.e.*, FITC was used to

bind mostly proteins (myocytes) and BODIPY to bind lipids (adipocytes). DIC and confocal microscopy images were used to confirm the dual staining process in the tissue (Fig. 5b and c). By tuning the pump light focal position, we were able to achieve lasing emission by scanning along the tissue in one direction, as shown in the dotted lines in Fig. 5b and c. Here, we chose 3 sites to represent two different tissues: site 1 (muscle tissue with 2 mM FITC), site 2 (adipose tissue with 1 mM BODIPY), and site 3 (muscle tissue with 2 mM FITC). Fig. 5d shows the conventional fluorescence spectra measured at sites 1, 2, and 3 (in the absence of the FP cavity by removing the top mirror). Apparently, we would not be able to distinguish the tissue type among these three sites by their fluorescence, thanks to the huge spectral overlap between FITC and BODIPY. In contrast, by placing the same tissue in the FP cavity (by putting the top mirror back), lasing signals (and hence the tissue type) of these three sites can be distinguished in Fig. 5e and f. Fig. 5e shows the selective lasing emission from only one type of tissue (and dye). In this case, the pump energy density ($20 \mu\text{J mm}^{-2}$) was set between the thresholds for FITC and BODIPY. Only lasing signals from FITC (site 1 and site 3) were generated. No laser signals could be detected from BODIPY (site 2). Since the mirror blocks a significant amount of fluorescence background and allows only the laser emission to pass, an extremely high contrast ratio ($\sim 10^3$) between sites 1 and 2 can be achieved. For comparison, the contrast of fluorescence between site 1 and site 2 is nearly unity (see Fig. 5d). Fig. 5f demonstrates the multiplexed lasing emission from multiple dyes. In this case, a higher pump energy density ($60 \mu\text{J mm}^{-2}$) was used to obtain the lasing emission from both FITC and BODIPY. Despite the strong spectral overlap in fluorescence, the lasing spectra from FITC and BODIPY are vastly different spectrally, thus allowing for clear differentiation between muscle and adipose tissues. The above two examples attest to the ability of the tissue laser to control and distinguish lasing signals in the presence of multiple dyes. Such an

ability arises from the sensitive dependence of the laser characteristics (such as lasing wavelength and threshold, as well as output intensity and polarization) on the emission/absorption properties of dyes and their biochemical and physical environment (such as tissue scattering/absorption and binding affinity of dyes to particular markers on tissue, *etc.*), which enables highly multiplexed analysis of tissues using various fluorophores. In addition to spectrally resolving two very similar dyes, the tissue laser provides another benefit, *i.e.*, high SBR. As exemplified in Fig. S9,§ the SBR in the tissue laser is 500, about 50-fold improvement over conventional fluorescence-based detection. Note that since the random laser does not have a mirror,^{17–21} strong fluorescence or scattering background will still be detected without being blocked, thus significantly reducing the SBR.

In many applications, fluorophores are conjugated to biochemical molecules in order to specifically bind to the target in a tissue. To demonstrate that the tissue lasing technique can be applied to fluorophore conjugates, we employed FITC–phalloidin as a model system, which has high affinity for F-actin in muscle tissues, as shown in Fig. 6.⁵⁴ In this experiment, lasing could be achieved by using only $10 \mu\text{M}$ FITC–phalloidin to stain the muscle tissue (Fig. S10§). In comparison with non-specific binding of FITC (Fig. 1f), the specific binding of FITC–phalloidin to F-actin resulted in localized fluorescence near cell membranes under a confocal microscope (Fig. 6a) and made the FITC concentration in the muscle tissue much higher than the original staining FITC–phalloidin concentration ($10 \mu\text{M}$). Consequently, lasing from FITC could be achieved with a threshold of about $130 \mu\text{J mm}^{-2}$ (Fig. 6b), while no lasing was observed with non-specific FITC in muscle tissue even at $300 \mu\text{J mm}^{-2}$ under the same conditions and using the same staining FITC concentration ($10 \mu\text{M}$). Based on our simulation in Fig. S3b,§ the effective FITC–phalloidin concentration inside the tissue is estimated to be $\sim 200 \mu\text{M}$. In Fig. 6c, the spatial distribution of the laser profiles suggests

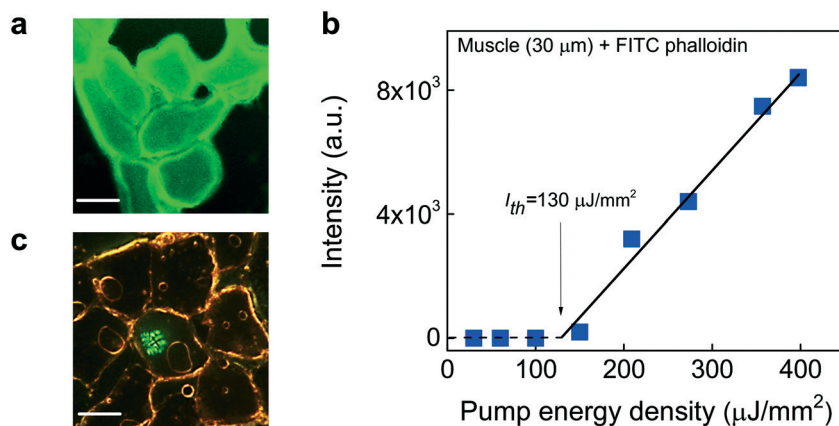


Fig. 6 Lasing in muscle tissue with FITC conjugates. a, Confocal fluorescence image of the muscle tissue stained with FITC–phalloidin. The muscle was arranged longitudinally. b, Spectrally integrated (530–545 nm) laser output as a function of pump energy density extracted from Fig. S10.§ The solid line is the linear fit above the threshold, which is approximately $130 \mu\text{J mm}^{-2}$. c, CCD image of lasing emission above the lasing threshold. All scale bars, 20 μm . Tissue thickness = 30 μm . [FITC–phalloidin] = 10 μM . Excitation wavelength = 465 nm.

that the lasing is a generalized higher order Ince–Gaussian mode.

In all the experiments presented so far, we used the plano–plano (p–p) FP cavity, which is well known to be unstable and susceptible to Q -factor degradation even with slight misalignment,^{38,55} and might also have contributed to the variations in the lasing threshold for different tissue thicknesses in Fig. 2e. Such Q -factor degradation is less significant in the case of single-cell lasers due to the lensing effect of the cell.¹⁴ Unfortunately, this lensing effect may not exist for tissue lasers when cells are embedded in the extracellular matrix. In contrast, plano–concave (p–c) FP cavities are highly stable and the high Q -factor can be maintained even with misalignment during assembly of the FP tissue laser. As a proof of concept, we created an array of micron-sized concave mirrors (3 mm apart between two adjacent concave mirrors) using CO₂ laser ablation on the same top mirror³⁸ (see Fig. S1§) and tested with the same FITC-stained muscle tissue. The Q -factor of those p–c FP cavities exceeded 10^5 , according to our previous work.³⁸ As shown in Fig. S11,§ a lasing threshold of approximately $2 \mu\text{J mm}^{-2}$ was achieved, ~ 10 times lower than that for the corresponding p–p FP cavity in Fig. 2 and about 100 times lower than that for the random tissue laser ($90\text{--}380 \mu\text{J mm}^{-2}$).^{18,20,24} Currently, our top mirror design does not allow us to scan the concave mirror. In the future, a high- Q scanning concave mirror can be created on the tip of an optical fiber^{56,57} to examine the entire tissue.

4. Conclusion

In this work, we have studied and developed a highly versatile tissue laser platform based on a high- Q FP cavity. Although only two dyes and two types of tissues were demonstrated in the current studies, there is no doubt that the tissue laser platform can readily be translated to other fluorophores (such as quantum dots⁵⁸ and fluorescent proteins) and other types of tissues. Such a tissue laser offers narrow spectral bandwidth, strong emission intensity, and large background rejection, which, coupled with the positive feedback provided by the laser cavity, can significantly improve the sensitivity, specificity, multiplexibility, and imaging contrast in tissue characterization. Besides emission intensity, the laser output from tissues consists of a number of unconventional parameters that can be monitored and serve as the sensing signal, such as the lasing threshold, lasing efficiency, and lasing mode spatial distribution. Collectively, the multi-parameter analysis would enable better understanding of intratissue/intertissue biological activities and structures.

In the near future, a few research directions will be explored towards eventual practical use of the tissue laser. First, a scanning concave mirror will be fabricated on an optical fiber facet, which allows us to scan over the tissue. Second, integration with an imaging spectrometer will be implemented for advanced tissue mapping with higher spectral and spatial information. Third, currently the FP tissue la-

ser is operated in a multi-mode regime. While the lasing emission band is much narrower than that in fluorescence, it is still about 10 nm wide, which limits the multiplexing capability. Eventually, a single-mode tissue laser will be pursued using either shorter cavity length or external optical feedback, in which case the lasing band can be far below 1 nm (currently ~ 0.2 nm, limited by the spectrometer resolution). Finally, fluorophores conjugated with antibodies can be used to target multiple biomarkers in tissues. We envision that our tissue laser will provide a novel spectroscopic tool for a plethora of applications ranging from medical diagnostics and preclinical drug testing to monitoring and identification of biological transformations in tissue engineering.

Acknowledgements

We acknowledge the support from the National Science Foundation (ECCS-1607250), the National Institutes of Health (NIBIB-1R21EB016783), and the National Science Foundation of China (Grant No. 61471254). We also thank the support of the Molecular Imaging Analysis Core Lab at the University of Michigan for assistance in cryostats and confocal microscopy and Dr. Gang Yao for discussion.

References

- 1 X. Fan and S.-H. Yun, The potential of optofluidic biolasers, *Nat. Methods*, 2014, **11**, 141–147.
- 2 M. C. Gather and S. H. Yun, Bio-optimized energy transfer in densely packed fluorescent protein enables nearmaximal luminescence and solid-state lasers, *Nat. Commun.*, 2014, **5**, 5722.
- 3 Q. Chen, *et al.*, Highly sensitive fluorescent protein FRET detection using optofluidic lasers, *Lab Chip*, 2013, **13**, 2679–2681.
- 4 A. Jonáš, *et al.*, In vitro and in vivo biolasing of fluorescent proteins suspended in liquid microdroplet cavities, *Lab Chip*, 2014, **14**, 3093–3100.
- 5 S. Nizamoglu, M. C. Gather and S. H. Yun, All-Biomaterial Laser using Vitamin and Biopolymers, *Adv. Mater.*, 2013, **25**, 5943–5947.
- 6 X. Wu, Q. Chen, Y. Sun and X. Fan, Bio-inspired optofluidic lasers with luciferin, *Appl. Phys. Lett.*, 2013, **102**, 203706.
- 7 Y. Sun, S. I. Shopova, C.-S. Wu, S. Arnold and X. Fan, Bioinspired optofluidic FRET lasers via DNA scaffolds, *Proc. Natl. Acad. Sci. U. S. A.*, 2010, **107**, 16039–16042.
- 8 W. Lee and X. Fan, Intracavity DNA Melting Analysis with Optofluidic Lasers, *Anal. Chem.*, 2012, **84**, 9558–9563.
- 9 X. Zhang, W. Lee and X. Fan, Bio-switchable Optofluidic Lasers Based on DNA Holliday Junctions, *Lab Chip*, 2012, **12**, 3673–3675.
- 10 Q. Chen, *et al.*, Self-assembled DNA tetrahedral optofluidic lasers with precise and tunable gain control, *Lab Chip*, 2013, **13**, 3351–3354.
- 11 P. L. Gourley, Biocavity laser for high-speed cell and tumour biology, *J. Phys. D: Appl. Phys.*, 2003, **36**, R228.

- 12 M. C. Gather and S. H. Yun, Single-cell biological lasers, *Nat. Photonics*, 2011, 5, 406–410.
- 13 M. Humar and S. H. Yun, Intracellular microlasers, *Nat. Photonics*, 2015, 9, 572–576.
- 14 M. Humar, M. C. Gather and S.-H. Yun, Cellular dye lasers: lasing thresholds and sensing in a planar resonator, *Opt. Express*, 2015, 23, 27865–27879.
- 15 M. Schubert, *et al.*, Lasing within live cells containing intracellular optical micro-resonators for barcode-type cell tagging and tracking, *Nano Lett.*, 2015, 15, 5647–5652.
- 16 Y.-C. Chen, Q. Chen and X. Fan, Lasing in blood, *Optica*, 2016, 3, 809–815.
- 17 X. Liu, *et al.*, Random laser action from a natural flexible biomembrane-based device, *J. Mod. Opt.*, 2016, 63, 1248–1253.
- 18 Q. Song, *et al.*, Random lasing in bone tissue, *Opt. Lett.*, 2010, 35, 1425–1427.
- 19 C.-S. Wang, T.-Y. Chang, T.-Y. Lin and Y.-F. Chen, Biologically inspired flexible quasi-single-mode random laser: An integration of *Pieris canidia* butterfly wing and semiconductors, *Sci. Rep.*, 2014, 4, 6736.
- 20 R. C. Polson and Z. V. Vardeny, Random lasing in human tissues, *Appl. Phys. Lett.*, 2004, 85, 1289–1291.
- 21 R. Polson and Z. V. Vardeny, Cancerous tissue mapping from random lasing emission spectra, *J. Opt.*, 2010, 12, 024010.
- 22 Y.-C. Chen, Q. Chen and X. Fan, Optofluidic chlorophyll lasers, *Lab Chip*, 2016, 16, 2228–2235.
- 23 S. Nizamoglu, *et al.*, A Simple Approach to Biological Single-Cell Lasers Via Intracellular Dyes, *Adv. Opt. Mater.*, 2015, 3, 1197–1200.
- 24 S. Caixeiro, M. Gaio, B. Marelli, F. G. Omenetto and R. Sapienza, Silk-Based Biocompatible Random Lasing, *Adv. Opt. Mater.*, 2016, 4, 998–1003.
- 25 Y. Sun and X. Fan, Distinguishing DNA by Analog-to-Digital-like Conversion by Using Optofluidic Lasers, *Angew. Chem., Int. Ed.*, 2012, 51, 1236–1239.
- 26 M. C. Gather and S. H. Yun, Lasing from *Escherichia Coli* Bacteria Genetically Programmed to Express Green Fluorescent protein, *Opt. Lett.*, 2011, 36, 3299–3301.
- 27 U. Bog, *et al.*, On-chip microlasers for biomolecular detection via highly localized deposition of a multifunctional phospholipid ink, *Lab Chip*, 2013, 13, 2701–2707.
- 28 Q. Chen, M. Ritt, S. Sivaramakrishnan, Y. Sun and X. Fan, Optofluidic lasers with a single molecular layer of gain, *Lab Chip*, 2014, 14, 4590–4595.
- 29 X. Wu, *et al.*, Optofluidic laser for dual-mode sensitive biomolecular detection with a large dynamic range, *Nat. Commun.*, 2014, 5, 3779.
- 30 M. Aas, Q. Chen, A. Jonáš, A. Kiraz and X. Fan, Optofluidic FRET lasers and their applications in novel photonic devices and biochemical sensing, *IEEE J. Sel. Top. Quantum Electron.*, 2016, 22, 1–15.
- 31 A. B. Chinen, *et al.*, Nanoparticle probes for the detection of cancer biomarkers, cells, and tissues by fluorescence, *Chem. Rev.*, 2015, 115, 10530–10574.
- 32 M. Vendrell, K. K. Maiti, K. Dhaliwal and Y.-T. Chang, Surface-enhanced Raman scattering in cancer detection and imaging, *Trends Biotechnol.*, 2013, 31, 249–257.
- 33 M. Muthana, *et al.*, Directing cell therapy to anatomic target sites in vivo with magnetic resonance targeting, *Nat. Commun.*, 2015, 6, 8009.
- 34 A. Orth, M. J. Tomaszewski, R. N. Ghosh and E. Schonbrun, Gigapixel multispectral microscopy, *Optica*, 2015, 2, 654–662.
- 35 M. J. Gerdes, *et al.*, Highly multiplexed single-cell analysis of formalin-fixed, paraffin-embedded cancer tissue, *Proc. Natl. Acad. Sci. U. S. A.*, 2013, 110, 11982–11987.
- 36 L. Zhou, *et al.*, Single-band upconversion nanoprobe for multiplexed simultaneous in situ molecular mapping of cancer biomarkers, *Nat. Commun.*, 2015, 6, 6938.
- 37 C. L. Zavaleta, *et al.*, Multiplexed imaging of surface enhanced Raman scattering nanotags in living mice using noninvasive Raman spectroscopy, *Proc. Natl. Acad. Sci. USA*, 2009, 106, 13511–13516.
- 38 W. Wang, *et al.*, Optofluidic laser array based on stable high-Q Fabry–Pérot microcavities, *Lab Chip*, 2015, 15, 3862–3869.
- 39 B. A. Clark, M. Alloosh, J. W. Wenzel, M. Sturek and T. Y. Kostrominova, Effect of diet-induced obesity and metabolic syndrome on skeletal muscles of Ossabaw miniature swine, *Am. J. Physiol.*, 2011, 300, E848–E857.
- 40 E. E. Spangenburg, S. J. Pratt, L. M. Wohlers and R. M. Lovering, Use of BODIPY (493/503) to visualize intramuscular lipid droplets in skeletal muscle, *BioMed. Res. Int.*, 2011, 2011, 598358.
- 41 D. R. Scriven, P. Dan and E. D. Moore, Distribution of proteins implicated in excitation-contraction coupling in rat ventricular myocytes, *Biophys. J.*, 2000, 79, 2682–2691.
- 42 E. Bedner, *et al.*, High affinity binding of fluorescein isothiocyanate to eosinophils detected by laser scanning cytometry: a potential source of error in analysis of blood samples utilizing fluorescein-conjugated reagents in flow cytometry, *Cytometry*, 1999, 36, 77–82.
- 43 S. R. Agarwal, C. E. Clancy and R. D. Harvey, Mechanisms restricting diffusion of intracellular cAMP, *Sci. Rep.*, 2016, 6, 19577.
- 44 J. C. Galas, C. Peroz, Q. Kou and Y. Chen, Microfluidic dye laser intracavity absorption, *Appl. Phys. Lett.*, 2006, 89, 224101.
- 45 Z. Li, Z. Zhang, T. Emery, A. Scherer and D. Psaltis, Single mode optofluidic distributed feedback dye laser, *Opt. Express*, 2006, 14, 696–701.
- 46 B. Helbo, A. Kristensen and A. Menon, A micro-cavity fluidic dye laser, *J. Micromech. Microeng.*, 2003, 13, 307–311.
- 47 G. Marquez, L. V. Wang, S.-P. Lin, J. A. Schwartz and S. L. Thomsen, Anisotropy in the absorption and scattering spectra of chicken breast tissue, *Appl. Opt.*, 1998, 37, 798–804.
- 48 M. A. Bandres and J. C. Gutiérrez-Vega, Ince–Gaussian beams, *Opt. Lett.*, 2004, 29, 144–146.
- 49 U. T. Schwarz, M. A. Bandres and J. C. Gutiérrez-Vega, Observation of Ince–Gaussian modes in stable resonators, *Opt. Lett.*, 2004, 29, 1870–1872.

- 50 G. Tearney, *et al.*, Determination of the refractive index of highly scattering human tissue by optical coherence tomography, *Opt. Lett.*, 1995, **20**, 2258–2260.
- 51 A. Kienle and R. Hibst, Light guiding in biological tissue due to scattering, *Phys. Rev. Lett.*, 2006, **97**, 018104.
- 52 J. Ranasinghesagara and G. Yao, Effects of inhomogeneous myofibril morphology on optical diffraction in single muscle fibers, *J. Opt. Soc. Am. A*, 2008, **25**, 3051–3058.
- 53 J. D. Atencio, S. V. y Montiel and S. Jacques, *Monte Carlo modeling of light propagation in neonatal skin*, INTECH Open Access Publisher, 2011.
- 54 C. P. Mack, A. V. Somlyo, M. Hautmann, A. P. Somlyo and G. K. Owens, Smooth muscle differentiation marker gene expression is regulated by RhoA-mediated actin polymerization, *J. Biol. Chem.*, 2001, **276**, 341–347.
- 55 A. E. Siegman, *Lasers*, University Science Books, 1986.
- 56 D. Hunger, *et al.*, A fiber Fabry-Perot cavity with high finesse, *New J. Phys.*, 2010, **12**, 065038.
- 57 D. Hunger, C. Deutsch, R. J. Barbour, R. J. Warburton and J. Reichel, Laser micro-fabrication of concave, low roughness features in silica, *AIP Adv.*, 2012, **2**, 012119.
- 58 A. Kiraz, Q. Chen and X. Fan, Optofluidic Lasers with Aqueous Quantum Dots, *ACS Photonics*, 2015, **2**, 707–713.